A coupled meshless-finite element method for fracture analysis of cracks

B.N. Rao, S. Rahman[1],*

College of Engineering, The University of Iowa, 2140 Seamans Center, Iowa City, IA 52242, USA

Abstract

This paper presents a coupling technique for integrating the element-free Galerkin method (EFGM) with the traditional finite element method (FEM) for analyzing linear-elastic cracked structures subject to mode-I and mixed-mode loading conditions. The EFGM was used to model material behavior close to cracks and the FEM in areas away from cracks. In the interface region, the resulting shape function, which comprises both EFGM and FEM shape functions, satisfies the consistency condition thus ensuring convergence of the method. The proposed method was applied to calculate mode-I and mode-II stress–intensity factors (SIFs) in a number of two-dimensional cracked structures. The SIFs predicted by this method compare very well with the existing solutions obtained by all-FEM or all-EFGM analyses. A significant saving of computational effort can be achieved due to coupling in the proposed method when compared with the existing meshless methods. Furthermore, the coupled EFGM–FEM method was applied to model crack propagation under mixed-mode loading condition. Since the method is partly meshless, a structured mesh is not required in the vicinity of the cracks. Only a scattered set of nodal points is required in the domain of interest. A growing crack can be modeled by simply extending the free surfaces, which correspond to a crack. By sidestepping remeshing requirements, crack-propagation analysis can be dramatically simplified. A number of mixed-mode problems were studied to simulate crack propagation. The agreement between the predicted crack trajectories with those obtained from existing numerical simulation and experiments are excellent. © 2001 Elsevier Science Ltd. All rights reserved.

Keywords: Element-free Galerkin method; Finite element method; Stress–intensity factor; Interaction integral; Crack propagation and linear-elastic fracture mechanics

1. Introduction

In recent years, a class of meshfree or meshless methods, such as smooth particle hydrodynamics [1–3], the diffuse element method [4], the element-free Galerkin method (EFGM) [5–7], h–p clouds [8], partition of unity [9], and the reproducing kernel particle method (RKPM) [10–12] has emerged to demonstrate significant potential for solving moving boundary problems typified by growing cracks. Fundamental to all meshless methods, a structured mesh is not used, since only a scattered set of nodal points is required in the domain of interest. This feature presents significant implications for modeling fracture propagation, because the domain of interest is completely discretized by a set of nodes. Since no element connectivity data are needed, the burdensome remeshing required by the finite element method (FEM) is avoided. A growing crack can be modeled by simply extending the free surfaces, which correspond to the crack. By sidestepping remeshing requirements, crack-propagation analysis can be dramatically simplified.

Although meshless methods are attractive for simulating crack propagation, because of the versatility, the computational cost of a meshless method typically exceeds the cost of a regular FEM. Furthermore, given the level of maturity and comprehensive capabilities of FEM, it is often advantageous to use meshless methods only in the sub-domains, where their capabilities can be exploited to the greatest benefit. In modeling crack propagation in a complex engineering structure with stiffeners, connections, welds, etc., it is more effective to apply meshless methods at the sites of potential crack growth and FEM in the remainder of the domain. Therefore, numerical methods need to be developed for combining meshless and finite element methods.

Several authors have already proposed different techniques to couple meshless and finite element methods. One technique, proposed by Krongauz and Belytschko [13] encircled the EFGM domain with the FEM domain and applied the boundary conditions to the finite element nodes. This coupling technique dramatically simplifies the enforcement of boundary conditions. These techniques, however, require a linear ramp function, which involves

* Corresponding author. Tel.: +1-319-335-5679; fax: +1-319-335-5669.
  E-mail address: rahman@engineering.uiowa.edu (S. Rahman).
[1] Website: http://www.engineering.uiowa.edu/~rahman.

substitution of finite element nodes with meshless nodes. In addition, the transition length is of one finite element. Subsequently, Hegen [14] employed Lagrange multipliers to couple the finite element and meshless regions. Later Liu et al. [11,12] proposed a method to adapt finite elements to the RKPM and multiresolution analysis, using different formulations. Recently, Huerta and Fernandez-Mendez [15] have presented a mixed hierarchical approximation for enrichment and coupling of the finite element and meshless methods. Indeed, combination of a meshless method and a FEM method continues to be a subject of great interest to many researchers.

In this paper, a numerical technique integrating EFGM with the traditional FEM is presented for analyzing linear-elastic cracked structures subject to mode-I and mixed-mode loading conditions. The EFGM is used to model material behavior close to cracks and the FEM in areas away from cracks. In the interface region, the resulting shape function, which comprises both EFGM and FEM shape functions, satisfies the consistency condition thus ensuring convergence of the method. Several numerical examples are presented to illustrate the proposed method by calculating mode-I and mode-II stress–intensity factors (SIFs) in two-dimensional cracked structures. For crack-propagation analysis, a number of mixed-mode problems are also presented to evaluate the accuracy and efficiency of the proposed coupled EFGM–FEM.

2. Element-free Galerkin method

Consider a function $u(\mathbf{x})$ over a domain $\Omega \subseteq \Re^K$, where $K = 1, 2,$ or 3. Let $\Omega_\mathbf{x} \subseteq \Omega$ denote a sub-domain describing the neighborhood of a point $\mathbf{x} \in \Re^K$ located in Ω. According to the moving least-squares (MLS) [16], the approximation $u^h(\mathbf{x})$ of $u(\mathbf{x})$ is

$$u^h(\mathbf{x}) = \sum_{I=1}^{N} \Phi_I(\mathbf{x}) d_I = \mathbf{\Phi}^T(\mathbf{x})\mathbf{d} \tag{1}$$

where $\mathbf{d}^T = \{d_1, ..., d_N\}$ and $\mathbf{\Phi}^T(\mathbf{x}) = \{\Phi_1(\mathbf{x}), \Phi_2(\mathbf{x}), ... \Phi_n(\mathbf{x})\}$ with d_I representing the nodal parameter (not the nodal values of $u^h(\mathbf{x})$) for node I and $\Phi_I(\mathbf{x})$ representing the MLS shape function corresponding to node I, given by

$$\Phi_I(\mathbf{x}) = \mathbf{a}^T(\mathbf{x})\mathbf{p}(\mathbf{x}_I)w_I(\mathbf{x}) \tag{2}$$

where $\mathbf{a}(\mathbf{x})$ is a vector of unknown parameters, which can be determined by imposing reproducibility or consistency conditions, $\mathbf{p}^T(\mathbf{x}) = \{p_1(\mathbf{x}), p_2(\mathbf{x}), ..., p_m(\mathbf{x})\}$ is a vector of complete basis functions of order m, and $w_I(\mathbf{x})$ is the weight function associated with node I such that $w_I(\mathbf{x}) \geq 0$ for all $\mathbf{x}$ in the support $\Omega_\mathbf{x}$ of $w_I(\mathbf{x})$ and zero otherwise, where $\mathbf{x}_I$ denotes the coordinates of node I. In Eq. (1), N is the total number of meshless nodes.

According to the reproducibility conditions, $u^h(\mathbf{x})$ in Eq. (1) approximates exactly polynomials of degree equal to or less than m. Hence

$$p(\mathbf{x}) = \sum_{I=1}^{N} p(\mathbf{x}_I)\Phi_I(\mathbf{x}) = \sum_{I=1}^{N} p(\mathbf{x}_I)\Phi_I{}^T(\mathbf{x}) \tag{3}$$

Substituting $\Phi_I(\mathbf{x})$ from Eq. (2) in Eq. (3) gives

$$\mathbf{p}(\mathbf{x}) = \left[\sum_{I=1}^{N} \mathbf{p}(\mathbf{x}_I)\mathbf{p}^T(\mathbf{x}_I)w_I(\mathbf{x})\right]\mathbf{a}(\mathbf{x}) \tag{4}$$

From Eq. (4), $\mathbf{a}(\mathbf{x})$ can be obtained as

$$\mathbf{a}(\mathbf{x}) = \mathbf{A}^{-1}(\mathbf{x})\mathbf{p}(\mathbf{x}) \tag{5}$$

where

$$\mathbf{A}(\mathbf{x}) = \sum_{I=1}^{N} \mathbf{p}(\mathbf{x}_I)\mathbf{p}^T(\mathbf{x}_I)w_I(\mathbf{x}) \tag{6}$$

is an $m \times m$ matrix. Substituting the expression of $\mathbf{a}(\mathbf{x})$ in Eq. (2), the shape function $\Phi_I(\mathbf{x})$ can be obtained readily.

The partial derivatives of $\Phi_I(\mathbf{x})$ can be obtained as

$$\Phi_{I,i}(\mathbf{x}) = \mathbf{a}_{,i}^T(\mathbf{x})\mathbf{p}(\mathbf{x}_I)w_I(\mathbf{x}) + \mathbf{a}^T(\mathbf{x})\{\mathbf{p}(\mathbf{x}_I)w_I(\mathbf{x})\}_{,i} \tag{7}$$

where

$$\mathbf{a}_{,i}(\mathbf{x}) = \mathbf{A}_{,i}^{-1}(\mathbf{x})\mathbf{p}(\mathbf{x}) + \mathbf{A}^{-1}(\mathbf{x})\mathbf{p}_{,i}(\mathbf{x}) \tag{8}$$

In Eq. (8), $\mathbf{A}_{,i}^{-1}$ can be obtained as [17]

$$\mathbf{A}_{,i}^{-1} = -\mathbf{A}^{-1}\mathbf{A}_{,i}\mathbf{A}^{-1} \tag{9}$$

in which $()_{,i} = \dfrac{\partial()}{\partial x_i}$

3. Coupled meshless-finite element method

Consider the domain $\Omega = \Omega_{EFGM} \cup \Omega_{FEM}$, which comprises two non-overlapping subdomains Ω_{EFGM} and Ω_{FEM} and boundary Γ_b, as shown in Fig. 1. Depending on the location of a point $\mathbf{x} \in \Re^K$, the reproducibility condition given by Eq. (3) can be written as follows:

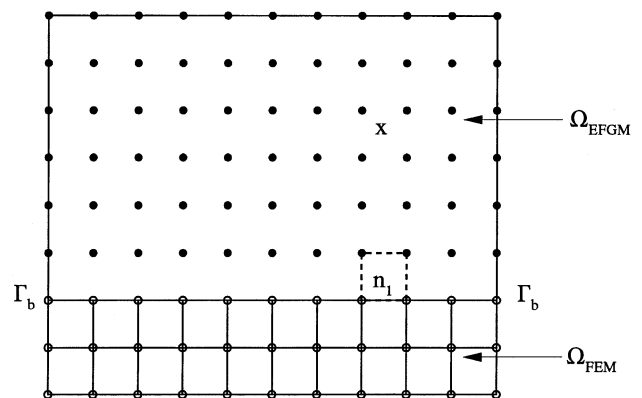**Case 1.** If $\mathbf{x} \in \Omega_{EFGM}$ and the shape function values of all

Fig. 1. Domain containing meshless and finite element zones.

FEM nodes are zero at $\mathbf{x}$

$$\mathbf{p}(\mathbf{x}) = \sum_{I=1,\mathbf{x}_I \in \Omega_{\text{EFGM}}}^{N} \mathbf{p}(\mathbf{x}_I)\Phi_I(\mathbf{x}) \tag{10}$$

in which the EFGM or MLS shape function $\Phi_I(\mathbf{x})$ and its partial derivatives can be obtained as explained in Section 2.

Case 2. A node on the boundary Γ_b, such as node n_1 in Fig. 1, is treated as an EFGM node or as a FEM node. Node n_1 is treated as a FEM node if its FEM shape function value obtained by forming a 4-noded quadrilateral element with an another neighboring FEM node on the boundary Γ_b along with two other EFGM nodes as shown by the dotted line in Fig.1, is nonzero at $\mathbf{x}$. Otherwise, node n_1 is treated as an EFGM node.

Hence, if $\mathbf{x} \in \Omega_{\text{EFGM}}$ and the shape function values of some FEM nodes along the boundary Γ_b are nonzero at $\mathbf{x}$

$$\mathbf{p}(\mathbf{x}) = \sum_{I=1,\mathbf{x}_I \in \Omega_{\text{EFGM}}}^{N} \mathbf{p}(\mathbf{x}_I)\Phi_I(\mathbf{x}) + \sum_{J=1,\mathbf{x}_J \in \Gamma_b}^{M} \mathbf{p}(\mathbf{x}_J)N_J(\mathbf{x}) \tag{11}$$

which can rewritten as

$$\mathbf{p}(\mathbf{x}) = \mathbf{A}(\mathbf{x})\mathbf{a}(\mathbf{x}) + \sum_{J=1,\mathbf{x}_J \in \Gamma_b}^{M} \mathbf{p}(\mathbf{x}_J)N_J(\mathbf{x}) \tag{12}$$

Hence

$$\mathbf{a}(\mathbf{x}) = \mathbf{A}^{-1}(\mathbf{x})\left\{ \mathbf{p}(\mathbf{x}) - \sum_{J=1,\mathbf{x}_J \in \Gamma_b}^{M} \mathbf{p}(\mathbf{x}_J)N_J(\mathbf{x}) \right\} \tag{13}$$

By substituting $\mathbf{a}(\mathbf{x})$ in Eq. (2), the shape function $\Phi_I(\mathbf{x})$ value can be obtained. The partial derivatives $\Phi_{I,i}(\mathbf{x})$ can be obtained as explained Section 2, using Eqs. (7)–(9).

Case 3. If $\mathbf{x} \in \Omega_{\text{FEM}}$

$$\mathbf{p}(\mathbf{x}) = \sum_{J=1,\mathbf{x}_J \in \Omega_{\text{FEM}}}^{M} \mathbf{p}(\mathbf{x}_J)N_J(\mathbf{x}) \tag{14}$$

where the FEM shape function $N_J(\mathbf{x})$ and its partial derivatives can be obtained by Lagrange interpolation [18].

Note, in Eqs. (10)–(14), $I = 1, ..., N$ are the EFGM nodes and $J = 1, ..., M$ are the FEM nodes.

Hence, the effective shape function for the coupled meshless-finite element method, denoted by $\tilde{\Phi}_I(\mathbf{x})$, can be defined as

Differentiating Eq. (15), the partial derivatives of effective shape function $\tilde{\Phi}_{I,i}(\mathbf{x})$ can be obtained. The effective shape function $\tilde{\Phi}_I(\mathbf{x})$ and its partial derivatives $\tilde{\Phi}_{I,i}(\mathbf{x})$ strongly depend on the type of basis function used. In this study the following fully enriched basis function [17,19] was used

$$\mathbf{p}^{\text{T}}(\mathbf{x}) = \left\{ 1, x_1, x_2, \sqrt{r}\cos\frac{\theta}{2}, \sqrt{r}\sin\frac{\theta}{2}, \right.$$
$$\left. \sqrt{r}\sin\frac{\theta}{2}\sin\theta, \sqrt{r}\cos\frac{\theta}{2}\sin\theta \right\} \tag{16}$$

where r and θ are polar coordinates with the crack tip as the origin.

4. Weight function

An important ingredient of EFGM or other meshless methods is the weight function $w(\mathbf{x})$. In this work, a weight function based on student's t-distribution [17], which represents the scaled probability density function of a standard Gaussian random variable divided by the square root of a chi-squared random variable with β degrees of freedom [20] was used. It is given by [17]

$$w_I(\mathbf{x}) = \begin{cases} \dfrac{\left(1 + \beta^2\dfrac{z_I^2}{z_{\text{m}I}^2}\right)^{-(1+\beta)/2} - (1 + \beta^2)^{-(1+\beta)/2}}{1 - (1 + \beta^2)^{-(1+\beta)/2}}, & z_I \le z_{\text{m}I} \\ 0, & z_I > z_{\text{m}I} \end{cases} \tag{17}$$

where β is the parameter controlling the shape of the weight function, $z_I = \|\mathbf{x} - \mathbf{x}_I\|$ is the distance from a sampling point $\mathbf{x}$ to a node $\mathbf{x}_I$, $z_{\text{m}I}$ is the domain of influence of node I such that

$$z_{\text{m}I} = z_{\max}z_{\text{c}I} \tag{18}$$

in which $z_{\text{c}I}$ is the characteristic nodal spacing distance which is chosen such that the node I has enough number of neighbors sufficient for regularity of $\mathbf{A}(\mathbf{x})$ in Eq. (6) (which is used to determine the MLS approximation), and $z_{\max}$ is a scaling parameter.

To avoid any discontinuities in the shape functions due to the presence of cracks, a diffraction method [19,21] can be used to modify z_I in the weight function. According to this method, when the line joining the node $\mathbf{x}_I$ to the sampling

$$\tilde{\Phi}_I(\mathbf{x}) = \begin{cases} \Phi_I(\mathbf{x}), & \text{if } \mathbf{x}_I \in \Omega_{\text{EFGM}} \\ N_I(\mathbf{x}), & \text{if } \mathbf{x}_I \in \Gamma_b \text{ and } N_I(\mathbf{x}) \ne 0 \\ \left\{ \mathbf{p}(\mathbf{x}) - \displaystyle\sum_{J=1,\mathbf{x}_J \in \Omega_{\text{FEM}}}^{M} \mathbf{p}(\mathbf{x}_J)N_J(\mathbf{x}) \right\}^{\text{T}} \mathbf{A}^{-1}(\mathbf{x})\mathbf{p}(\mathbf{x}_I)w_I(\mathbf{x}), & \text{if } \mathbf{x}_I \in \Gamma_b \text{ and } N_I(\mathbf{x}) = 0 \\ N_I(\mathbf{x}), & \text{if } \mathbf{x}_I \in \Omega_{\text{FEM}} \end{cases} \tag{15}$$

point $\mathbf{x}$ intersects the crack segment and the crack tip is within the domain of influence of the node $\mathbf{x}_I$, z_I is modified as [19]

$$z_I = \left(\frac{s_1 + s_2(\mathbf{x})}{s_0(\mathbf{x})} \right)^\lambda s_0(\mathbf{x}) \tag{19}$$

where $s_1 = \|\mathbf{x}_I - \mathbf{x}_c\|$, $s_2(\mathbf{x}) = \|\mathbf{x} - \mathbf{x}_c\|$, $s_0(\mathbf{x}) = \|\mathbf{x} - \mathbf{x}_I\|$, $\mathbf{x}$ and $\mathbf{x}_c$ are the coordinates of the sampling point and crack tip, respectively, and $1 \le \lambda \le 2$ is a parameter for adjusting the distance of the support on the opposite side of the crack.

5. Variational formulation and discretization

For small displacements in two-dimensional, homogeneous, isotropic, and linear-elastic solids, the equilibrium equations and boundary conditions are

$$\nabla\cdot\boldsymbol{\sigma} + \mathbf{b} = 0 \qquad \text{in } \Omega \tag{20}$$

and

$$\boldsymbol{\sigma}\cdot\mathbf{n} = \bar{\boldsymbol{t}} \quad \text{on} \quad \Gamma_t \ (\text{natural boundary conditions})$$
$$\mathbf{u} = \bar{\boldsymbol{u}} \quad \text{on} \quad \Gamma_u \ (\text{essential boundary conditions}) \tag{21}$$

respectively, where $\boldsymbol{\sigma} = \Delta\boldsymbol{\epsilon}$ is the stress vector, $\mathbf{D}, J$ the material property matrix, $\boldsymbol{\epsilon} = \nabla_s\mathbf{u}$ is the strain vector, $\mathbf{u}$ is the displacement vector, $\mathbf{b}$ is the body force vector, $\bar{\boldsymbol{t}}$ and $\bar{\boldsymbol{u}}$ are the vectors of prescribed surface tractions and displacements, respectively, $\mathbf{n}$ is a unit normal to domain, Ω, Γ_t and Γ_u are the portions of boundary Γ where tractions and displacements are prescribed, respectively, $\nabla^T = \{\partial/\partial x_1, \partial/\partial x_2\}$ is the vector of gradient operators, and $\nabla_s\mathbf{u}$ is the symmetric part of $\nabla\mathbf{u}$. The variational or weak form of Eqs. (20) and (21) is

$$\int_\Omega \boldsymbol{\sigma}^T\delta\boldsymbol{\epsilon}\, d\Omega - \int_\Omega \mathbf{b}^T\delta\mathbf{u}\, d\Omega - \int_{\Gamma_t} \bar{\boldsymbol{t}}^T\delta\mathbf{u}\, d\Gamma - \delta W_u = 0 \tag{22}$$

where δ denotes the variation operator and δW_u represents a term to enforce the essential boundary conditions, defined as

$$W_u = \sum_{J\in\Gamma_u} \mathbf{f}^T(\mathbf{x}_J)[\mathbf{u}(\mathbf{x}_J) - \bar{\boldsymbol{u}}(\mathbf{x}_J)] \tag{23}$$

where $\mathbf{f}^T(\mathbf{x}_J)$ is the vector of reaction forces at the constrained node $\mathbf{x}_J \in \Gamma_u$. Hence

$$\delta W_u = \sum_{J\in\Gamma_u} \delta\mathbf{f}^T(\mathbf{x}_J)[\mathbf{u}(\mathbf{x}_J) - \bar{\boldsymbol{u}}(\mathbf{x}_J)] + \mathbf{f}^T(\mathbf{x}_J)\delta\mathbf{u}(\mathbf{x}_J) \tag{24}$$

Consider a single boundary constraint, $\bar{u}_i(\mathbf{x}_J) = g_i(\mathbf{x}_J)$ applied at node J in the direction of the x_i coordinate. Then, the variational form given by Eqs. (22) and (24) can be expressed by

$$\int_\Omega \boldsymbol{\sigma}^T\delta\boldsymbol{\epsilon}\, d\Omega + f_i(\mathbf{x}_J)\delta u_i(\mathbf{x}_J) = \int_\Omega \mathbf{b}^T\delta\mathbf{u}\, d\Omega + \int_{\Gamma_t} \bar{\boldsymbol{t}}^T\delta\mathbf{u}\, d\Gamma \tag{25}$$

$$\delta f_i(\mathbf{x}_J)[u_i(\mathbf{x}_J) - g_i(\mathbf{x}_J)] = 0 \tag{26}$$

where $f_i(\mathbf{x}_J)$ and $u_i(\mathbf{x}_J)$ are the ith component of $\mathbf{f}(\mathbf{x}_J)$ and $\mathbf{u}(\mathbf{x}_J)$, respectively. Using the coupled meshless-finite element shape function $\tilde{\Phi}_I(\mathbf{x})$ the approximation of $u_i(\mathbf{x}_J)$ can be written as

$$u_i^h(\mathbf{x}_J) = \sum_{I=1}^N \tilde{\Phi}_I(\mathbf{x}_J)d_I^i = \tilde{\boldsymbol{\Phi}}_J^{iT}\mathbf{d} \tag{27}$$

where

$$\tilde{\boldsymbol{\Phi}}_J^{iT} = \begin{cases} \{\tilde{\Phi}_1(\mathbf{x}_J), 0, \tilde{\Phi}_2(\mathbf{x}_J), 0, ..., \tilde{\Phi}_N(\mathbf{x}_J), 0\}, & \text{when } i = 1 \\ \{0, \tilde{\Phi}_1(\mathbf{x}_J), 0, \tilde{\Phi}_2(\mathbf{x}_J), ..., 0, \tilde{\Phi}_N(\mathbf{x}_J)\}, & \text{when } i = 2 \end{cases} \tag{28}$$

and

$$\mathbf{d} = \begin{Bmatrix} d_1^1 \\ d_2^1 \\ d_1^2 \\ d_2^2 \\ \vdots \\ d_1^N \\ d_2^N \end{Bmatrix} \tag{29}$$

is the vector of nodal parameters or generalized displacements, and N is the total number of nodal points in Ω. The shape function values are computed as described in Section 4. Using Eqs. (27)–(29) into the discretization of Eqs. (25) and (26) gives [5–7]

$$\begin{bmatrix} \mathbf{k} & \tilde{\boldsymbol{\Phi}}_J^i \\ \tilde{\boldsymbol{\Phi}}_J^{iT} & 0 \end{bmatrix} \begin{Bmatrix} \mathbf{d} \\ f_i(\mathbf{x}_J) \end{Bmatrix} = \begin{Bmatrix} \mathbf{f}^{ext} \\ g_i(\mathbf{x}_J) \end{Bmatrix} \tag{30}$$

where

$$\mathbf{k} = \begin{bmatrix} \mathbf{k}_{11} & \mathbf{k}_{12} & ... & \mathbf{k}_{1N} \\ \mathbf{k}_{21} & \mathbf{k}_{22} & ... & \mathbf{k}_{2N} \\ \vdots & \vdots & \vdots & \vdots \\ \mathbf{k}_{N1} & \mathbf{k}_{N2} & ... & \mathbf{k}_{NN} \end{bmatrix} \in \mathscr{L}(\Re^{2N} \times \Re^{2N}) \tag{31}$$

is the stiffness matrix with

$$\mathbf{k}_{IJ} = \int_\Omega \mathbf{B}_I^T\mathbf{D}\mathbf{B}_J\, d\Omega \in \mathscr{L}(\Re^2 \times \Re^2) \tag{32}$$

representing the contributions of the Jth node at node I

$$\mathbf{f}^{ext} = \begin{Bmatrix} \mathbf{f}_1^{ext} \\ \mathbf{f}_2^{ext} \\ \vdots \\ \mathbf{f}_N^{ext} \end{Bmatrix} \in \Re^{2N} \tag{33}$$

is the force vector with

$$\mathbf{f}_I^{\text{ext}} = \int_\Omega \tilde{\Phi}_I \mathbf{b}^{\text{T}} \, d\Omega + \int_{\Gamma_t} \tilde{\Phi}_I \tilde{t}^{\text{T}} \, d\Gamma \in \Re^2 \tag{34}$$

$$\mathbf{B}_I = \begin{bmatrix} \tilde{\Phi}_{I,1} & 0 \\ 0 & \tilde{\Phi}_{I,2} \\ \tilde{\Phi}_{I,2} & \tilde{\Phi}_{I,1} \end{bmatrix} \tag{35}$$

and

$$\mathbf{D} = \begin{cases} \dfrac{E}{1-\nu^2} \begin{bmatrix} 1 & \nu & 0 \\ \nu & 1 & 0 \\ 0 & 0 & \dfrac{1-\nu}{2} \end{bmatrix}, & \text{for plane stress} \\[4pt] \dfrac{E}{(1+\nu)(1-2\nu)} \begin{bmatrix} 1-\nu & \nu & 0 \\ \nu & 1-\nu & 0 \\ 0 & 0 & \dfrac{1-2\nu}{2} \end{bmatrix}, & \text{for plane strain} \end{cases} \tag{36}$$

is the elasticity matrix with E and ν representing the elastic modulus and Poisson's ratio, respectively.

A transformation method [17,22] was used for solving the equilibrium equation (Eq. (30)).

6. Computational fracture mechanics

6.1. Calculation of stress–intensity factors

Consider a structure with a rectilinear crack of length $2a$ that is subjected to external stresses. Let K_{I} and K_{II} be the SIFs for mode-I and mode-II, respectively. These SIFs can be evaluated using the interaction integral [23] converted into a domain form [24]. For example

$$K_{\text{I}} = \frac{E'}{2} M^{(1,2)} \tag{37}$$

where

$$E' = \begin{cases} E, & \text{plane stress} \\ \dfrac{E}{1-\nu^2}, & \text{plane strain} \end{cases} \tag{38}$$

is the effective elastic modulus, and $M^{(1,2)}$ is the interaction integral. It includes the terms from the actual mixed mode state for the given boundary conditions (superscript1) and the super-imposed near-tip mode I auxiliary state (superscript 2). $M^{(1,2)}$ is given by

$$M^{(1,2)} = \int_A \left[\sigma_{ij}^{(1)} \frac{\partial u_i^{(2)}}{\partial x_1} + \sigma_{ij}^{(2)} \frac{\partial u_i^{(1)}}{\partial x_1} - W^{(1,2)} \delta_{1j} \right] \frac{\partial q}{\partial x_j} \, dA \tag{39}$$

where σ_{ij} and u_i are the components of the stress tensor and displacement vector, respectively, $W^{(1,2)}$ is the mutual strain energy from the two states and q is a weight function chosen such that it has a value of *unity* at the crack tip, *zero* along the boundary of the domain and arbitrary elsewhere. Note that all the quantities are evaluated with respect to a coordinate system with crack tip as origin. Following similar considerations K_{II} can be calculated from Eqs. (37)–(39), except that the near-tip mode II state is chosen as the auxiliary state while computing $M^{(1,2)}$.

6.2. Simulation of crack propagation

In order to simulate crack growth under linear-elastic condition, the crack-path direction must be determined. There are a number of criteria available to predict the direction of the crack trajectory. They are based on: (1) maximum circumferential stress [25], (2) minimum strain energy density [26], (3) maximum energy release rate [27], and (4) vanishing in-plane SIF (K_{II}) in shear mode for infinitesimally small crack extension [28]. The first two criteria predict the direction of crack trajectory from the stress state prior to the crack extension. The last two criteria require stress analysis for virtually extended cracks in various directions to find the appropriate crack-growth directions. In this study, the crack-growth simulation was based on the first criterion only. Other criteria, which are not considered here, can be easily implemented into the proposed coupled EFGM-FEM.

6.3. Crack trajectory prediction

According to the maximum circumferential stress criterion [25], the initial direction of crack propagation θ, is the solution of the equation

$$K_{\text{I}} \sin \theta + K_{\text{II}}(3 \cos \theta - 1) = 0 \tag{40}$$

where K_{I} and K_{II} are SIFs for any instant during the crack growth. When the values of K_{I} and K_{II} are known, θ can be easily solved using standard numerical procedures.

6.4. Quasi-automatic crack propagation

A fully automatic strategy for crack propagation is one, which requires no user interaction to predict both the extent and direction of crack growth. The present approach is, however, quasi-automatic because the user still needs to provide a desired crack-length increment every time the crack tip moves. The quasi-automatic simulation of crack propagation involves a number of successive analyses. Each analysis consists of the following steps:

1. A numerical analysis is performed to predict stress and strain fields
2. SIFs are calculated from the results of step 1.
3. The direction of crack trajectory is calculated from Eq. (40).
4. For a user-defined crack-length increment, the location of

the new crack-tip is determined. The crack geometry is updated.

5. The meshless node in the old crack-tip (if exists) is split into two nodes locating on the opposite sides of the crack.
6. New meshless nodes are added for improved discretization of the domain, if desired.

7. Numerical examples

The coupled meshless-FEM developed in this study was applied to perform fracture-mechanics analysis of both stationary and propagating cracks. Both single- (mode I) and mixed-mode (modes I and II) conditions were considered and four examples are presented here. The diffraction parameter value $\lambda = 1$ was used in all examples. For numerical integration, an 8×8 Gauss quadrature was used both in the meshless region and the FEM region for all the examples.

(a)

(b)
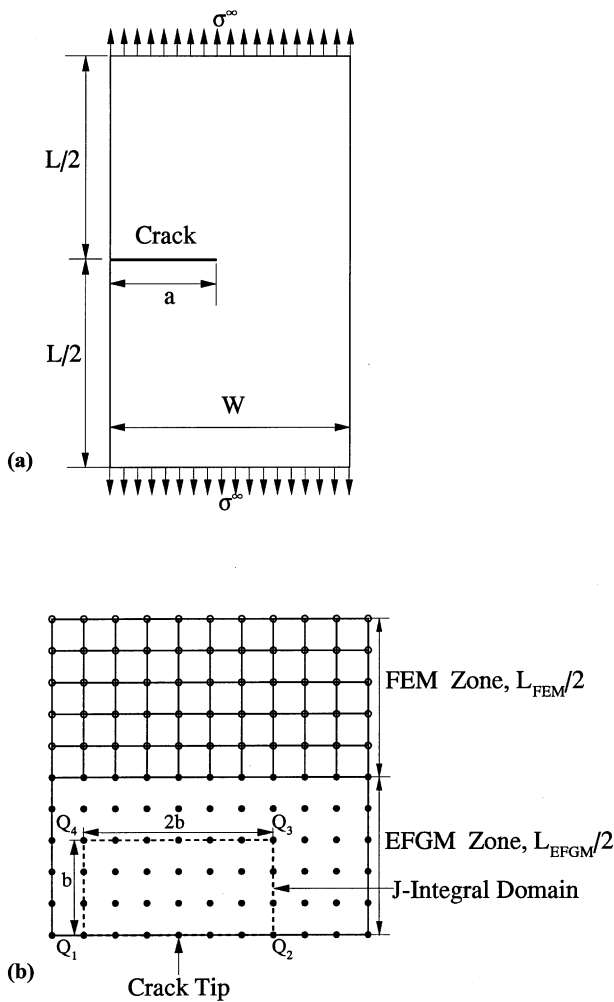
Fig. 2. Edge-cracked plate under mode-I loading: (a) geometry and loads; (b) domain discretization.

Table 1
Mode-I SIF for different lengths of EFGM zone (Example 1)

L_{EFGM}/L	K_I	SIF ratio[a]
0.8	2.3441	0.994
0.7	2.3359	0.991
0.6	2.3423	0.993
0.5	2.3569	1.000
0.4	2.3724	1.006
0.3	2.3867	1.012
0.2	2.3701	1.005
0.1	2.1644	0.918

[a] SIF ratio = predicted SIF/reference value of SIF. Reference values: $K_I = 2.358$ units [29].

Example 1. Stationary crack under mode-I

Consider an edge-cracked plate under pure tension as shown in Fig. 2(a), that has length $L = 2$ units, width $W = 1$ unit, and crack length $a = 0.4$ units. The far-field tensile stress $\sigma^\infty = 1$ unit. Due to symmetry, only half of the plate was analyzed. The half plate model consisting of 121 uniformly spaced nodes is shown in Fig. 2(b), some of which are treated as meshless nodes and the remainder are treated as 4-noded quadrilateral finite elements. In the meshless region the domain of the plate was divided into rectangular cells with their nodes coincident with the meshless nodes solely for numerical integration. A domain $Q_1Q_2Q_3Q_4$ of size $2b \times b$, required for calculating the J-integral is defined in Fig. 2(b). The domain size dimension $b = \{\min(0.4L_{EFGM}, a)\}$, where L_{EFGM} is the length of EFGM zone as shown in Fig. 2(b) and a is the crack length. A plane stress condition was assumed with $E = 207,000$ units and $\nu = 0.3$.

Table 1 shows the values of K_I for different values of L_{EFGM}/L. For the weight function, $\beta = 1$ was used for these calculations. For J-integral calculation domain size was chosen such that the entire domain was in the meshless region. When compared with the benchmark solution of $K_I = 2.358$ units, given by Tada et al. [29], the predicted values of K_I from the present study are accurate upto $L_{EFGM}/L = 0.2$. The accuracy of the predicted value of K_I degrades when $L_{EFGM}/L \leq 0.1$, due to the smaller sizes of meshless zone and the domain over which the J-integral integral is evaluated. It is worth mentioning that for large values of L_{EFGM}/L, the predicted values of K_I from the

Table 2
Mode-I SIF using various integral domains ($L_{EFGM}/L = 0.5$) (Example 1)

Size of domain ($2b \times b$)	K_I	SIF ratio[a]
0.80×0.40	2.3569	1.000
0.64×0.32	2.3406	0.993
0.60×0.30	2.3420	0.993
0.40×0.20	2.3005	0.976

[a] SIF ratio = predicted SIF/reference value of SIF. Reference values: $K_I = 2.358$ units [29].

Table 3
Mixed-mode stress-intensity factor for different lengths of EFGM zone
(Example 2)

L_{EFGM}/L	Mode-I		Mode-II	
	K_I	SIF ratio[a]	K_{II}	SIF ratio[a]
12/14	33.63	0.989	4.536	0.997
11/14	33.62	0.989	4.539	0.998
10/14	33.57	0.987	4.520	0.993
9/14	33.55	0.987	4.539	0.998
8/14	33.47	0.984	4.521	0.994
7/14	33.33	0.980	4.504	0.990
6/14	33.42	0.983	4.491	0.987
5/14	33.39	0.982	4.004	0.880
4/14	34.89	1.026	4.694	1.032
3/14	34.65	1.019	3.681	0.809
2/14	36.12	1.062	4.968	1.092

[a] SIF ratio = predicted SIF/reference value of SIF. Reference values:
$K_I = 34.0$ units and $K_{II} = 4.55$ units [31].

Table 4
Mixed-mode stress-intensity factor using various integral domains
($L_{EFGM}/L = 7/14$) (Example 2)

Size of domain $(2b_1 \times 2b_2)$	Mode-I		Mode-II	
	K_I	SIF ratio[a]	K_{II}	SIF ratio[a]
2.8×4.0	33.27	0.979	4.562	1.003
5.6×6.0	33.37	0.981	4.522	0.994
7.0×7.0	33.36	0.981	4.518	0.993

[a] SIF ratio = predicted SIF/reference value of SIF. Reference values:
$K_I = 34.0$ units and $K_{II} = 4.55$ units [31].

present study matches well with the available results in the literature involving EFGM analysis for the whole domain [5,17,30].

Table 2 shows the effect of the *J*-integral domain size on the predicted values of K_I when $L_{EFGM}/L = 0.5$. Very accurate results of SIF were obtained regardless of the size of the domain.

Example 2. Stationary crack under mixed-mode

This example involves an edge-cracked plate in Fig. 3(a), which is fixed at the bottom and subjected to far-field shear stress $\tau^\infty = 1$ unit applied on the top. The plate has length $L = 16$ units, width $W = 7$ units, and crack length $a = 3.5$ units. A domain of size $2b_1 \times 2b_2$ required for calculating $M^{(1,2)}$ integral is also shown in Fig. 3(a) and (b) shows the domain discretization involving 324 uniformly spaced nodes, some of which are treated as meshless nodes and the remainder are treated as 4-noded quadrilateral finite elements. In the meshless region, a background mesh with cell points coincident with the meshless nodes was used. The elastic modulus and Poisson's ratio were 30×10^6 units and 0.25, respectively. A plane strain condition was assumed. The mode-I and mode-II SIFs were calculated according to Eqs. (37)–(39).

Table 3 shows the predicted K_I and K_{II} for this edge-cracked problem using $\beta = 2$ for various values of L_{EFGM}/L. The domain size for $M^{(1,2)}$ integral calculation was chosen such that the entire domain was in the meshless region. The domain size dimensions were chosen as follows: $b_1 = b_2 = \{\min(0.4L_{EFGM}, a)\}$, where L_{EFGM} is defined as shown in the Fig. 3(b) and a is the crack length. The reference solutions for this problem are: $K_I = 34$ units and $K_{II} = 4.55$ units [31]. The predicted K_I and K_{II} values compare very well with the reference SIF values upto $L_{EFGM}/L = 6/14$. However, the accuracy of the predicted values deteriorates and oscillates when $L_{EFGM}/L \leq 5/14$, possibly due to the smaller meshless zone and size of the domain over
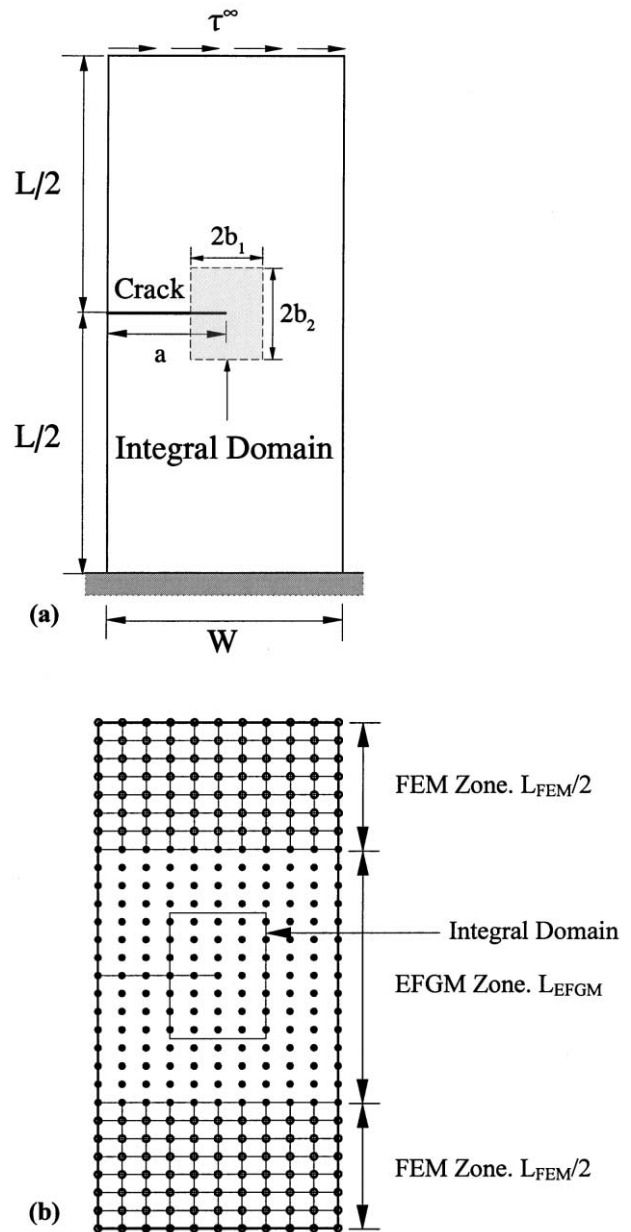

Fig. 3. Edge-cracked plate under mixed-mode loading: (a) geometry, loads, and domain size; (b) domain discretization.
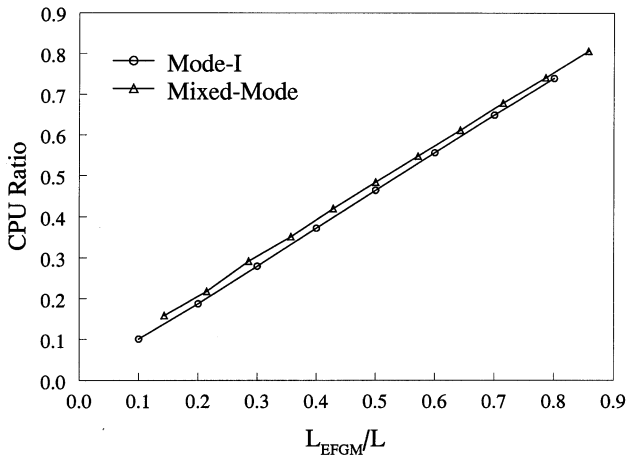
Fig. 4. Comparison of CPU time.

which the $M^{(1,2)}$ integral is evaluated. For large values of L_{EFGM}/L, the predicted K_I and K_{II} values from the present study matches well with the results of [17,19] based on EFGM analysis of the whole domain.

Table 4 shows the predicted K_I and K_{II} for this edge-cracked problem for various sizes of fracture integral domain when $L_{EFG}/L = 7/14$. No major effects of domain size are seen.

Fig. 4 plots variation of CPU ratio, defined as the ratio of CPU time using coupled meshless-FEM method and CPU time using meshless method for the whole domain. Fig. 4 includes both mode-I and mixed-mode cases. It is evident from the plot that CPU time decreases with decrease in L_{EFGM}/L, as expected. Hence combining the meshless method with FEM can significantly reduce computational effort for
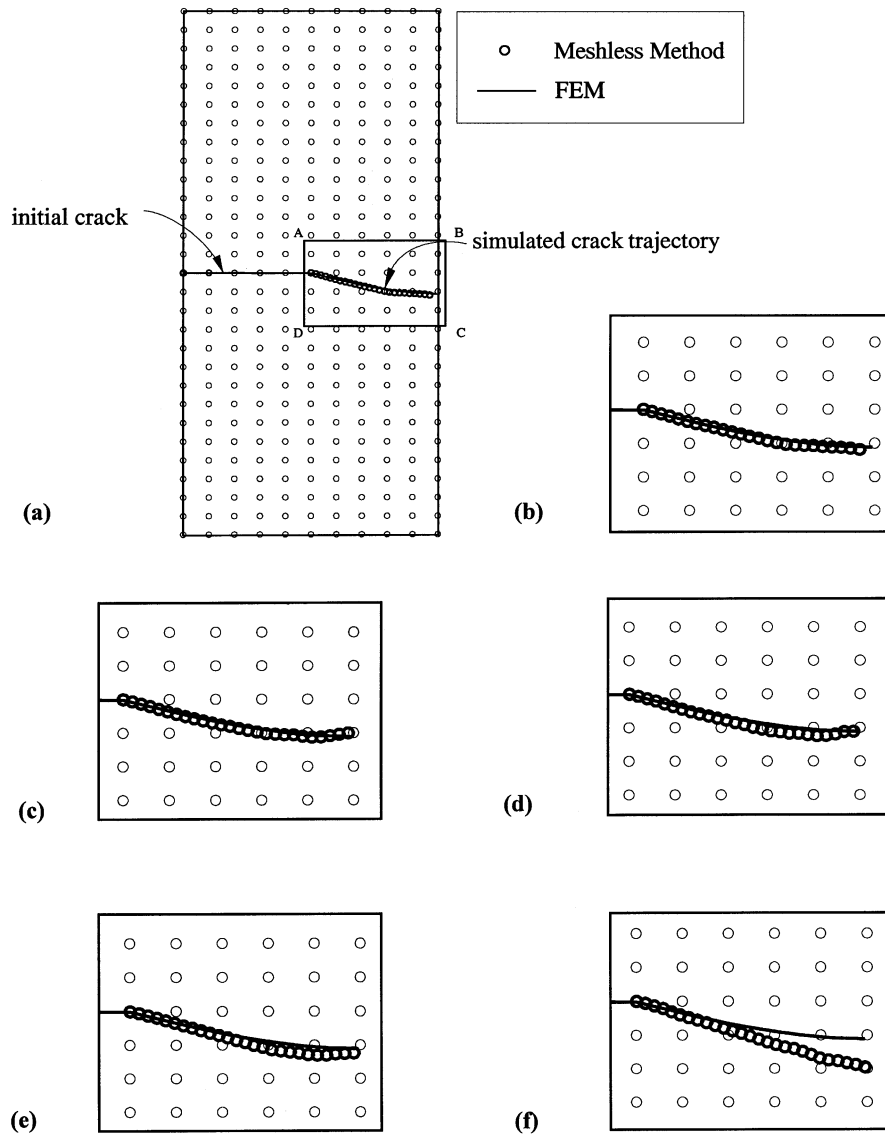

Fig. 5. Simulation of crack propagation: (a) meshless method for the whole domain ($L_{EFGM}/L = 1$); (b) $L_{EFGM}/L = 1$; (c) $L_{EFGM}/L = 7/14$; (d) $L_{EFGM}/L = 6/14$; (e) $L_{EFGM}/L = 5/14$; (f) $L_{EFGM}/L = 4/14$.

solving fracture mechanics problems, preserving the accuracy obtained by adopting EFGM for the whole domain.

Example 3. Propagating crack under mixed-mode

Consider the edge-crack problem as this example. In this example, the accuracy of crack-path prediction using the proposed technique is evaluated. A domain size of 0.9×0.9 units was used for meshless simulation. Otherwise, all other input parameters are the same as in Example 2. For crack-propagation analysis, the maximum circumferential stress criterion was used.

Fig. 5 shows the evolution of crack trajectory using the meshless method for the whole domain and the proposed coupled meshless-finite element method for the four cases $L_{\text{EFGM}}/L = 7/14$, 6/14, 5/14 and 4/14. The increment of crack length during each step of crack propagation was 4% of the initial crack length. At each increment, a new node was added at the crack tip. For comparison, a similar crack-growth analysis was performed using the FEM for the whole domain. The FEM involves quarter-point singularity elements and an automatic remeshing procedure for updating the crack-tip mesh during the progression of crack growth. Fig. 5(a) shows the comparison of the predicted crack trajectory using the meshless method for the whole domain with that obtained by using FEM for the whole domain. Fig. 5(b) shows an enlarged view of the region ABCD shown in Fig. 5(a). Fig. 5(c) through (f) shows the enlarged view of the comparison of the predicted crack trajectory using the proposed method with that obtained by using FEM for the whole domain, for the four cases $L_{\text{EFGM}}/L = 7/14$, 6/14, 5/14 and 4/14, respectively. The predicted crack path from the proposed method almost coincides with the crack path from FEM for $L_{\text{EFGM}}/L = 7/14$ and 6/14. Hence the accuracy of the crack trajectory is maintained without the burdensome remeshing required by FEM and at the same time, curtailing the computational expense of the meshless method. The proposed method can significantly reduce the complexity of crack-propagation analysis. The predicted crack path from the proposed method deviates from the crack path from FEM for $L_{\text{EFGM}}/L = 5/14$ and 4/14. This result is expected, since some error is observed in the predictions of K_{I} and K_{II} for these two cases using the coupled meshless-FEM.

Example 4. Experimental validation

In this example, crack trajectories predicted by the proposed method are compared with Pustejovsky's experimental data [32,33]. Pustejovsky performed a series of uniaxial tension tests on isotropic Titanium Ti–6Al–4V plates with oblique center-cracks of length $2a = 13.5$ mm at $\gamma = 43°$ and length $2a = 14.2$ mm at $\gamma = 30°$. The reported dimensions and material properties of the specimens were: length $2L = 304.8$ mm, width $2W = 76.2$ mm, elastic modulus $E = 110$ GPa and Poisson's ratio $\nu = 0.29$. A far-field uniaxial tensile stress, $\sigma^\infty = 207$ MPa was applied on the top and the bottom of the specimen during
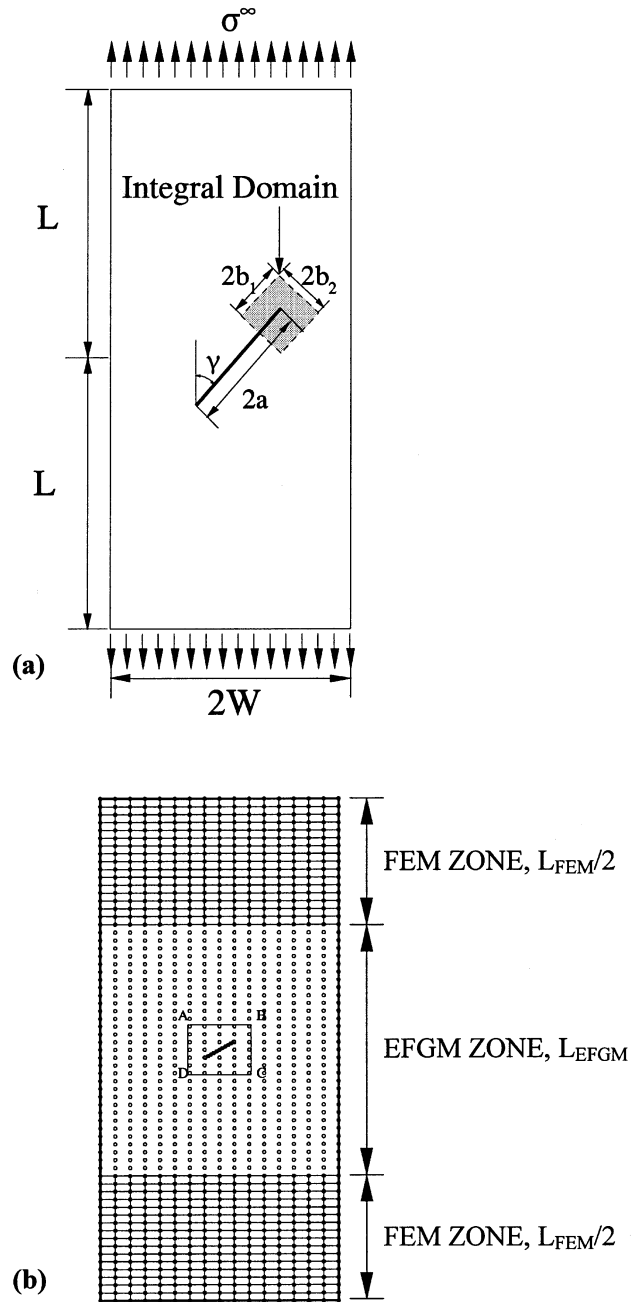

Fig. 6. Center oblique cracked titanium Ti-6Al-4V plate under uniaxial loading: (a) geometry, loads, and domain size; (b) domain discretization.

meshless analysis. Fig. 6(a) and (b) show the dimensions of the specimen and the meshless discretization, respectively. The domain discretization involves 1124 nodes, some of which are treated as meshless nodes and the remainder are treated as 4-noded quadrilateral finite elements. A hybrid enrichment of basis function was adopted by using fully enriched basis function for a small region close to the two crack tip regions and by using linear basis function for the rest of the meshless region. The inner radius of the coupling region for hybrid enrichment was $0.25a$ and the outer radius was $0.375a$. As shown in Fig. 6(a), a domain size
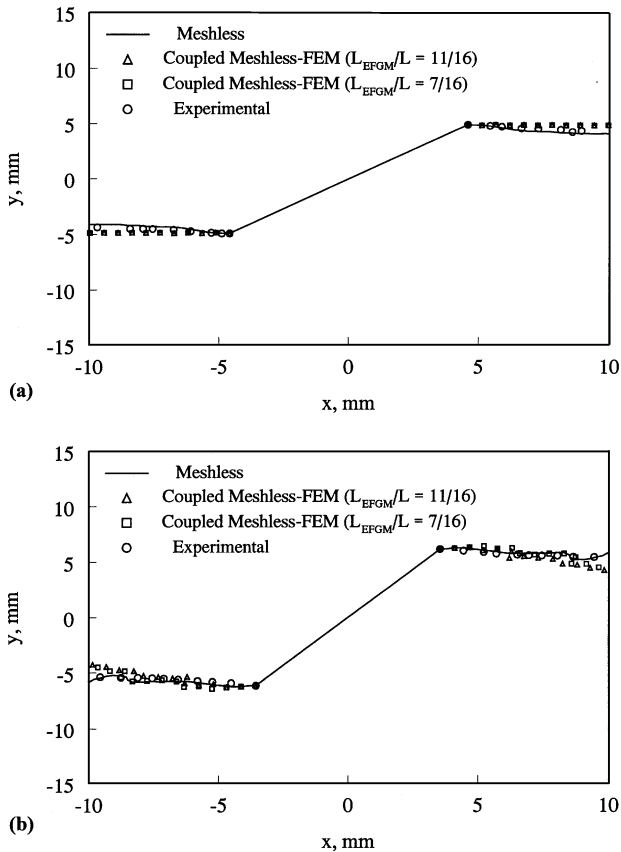
Fig. 7. Comparison of simulated crack trajectory with experimental data: (a) $\gamma = 43°$ and $2a = 13.5$ mm; (b) $\gamma = 30°$ and $2a = 14.2$ mm.

resulting shape function, which comprises both EFGM and FEM shape functions, satisfy the consistency condition thus ensuring convergence of the method. The proposed method was applied to calculate mode-I and mode-II SIFs in a number of two-dimensional cracked structures. The SIFs predicted by this method compare very well with the existing solutions obtained by all-FEM or all-EFGM analyses. A significant saving of computational effort can be achieved due to coupling in the proposed method when compared with the existing meshless methods. Furthermore, the coupled EFGM–FEM method was applied to model crack propagation under mixed-mode loading condition. Since the method is partly meshless, a structured mesh is not required in the vicinity of the cracks. Only a scattered set of nodal points is required in the domain of interest. By sidestepping remeshing requirements, crack-propagation analysis can be dramatically simplified. A number of mixed-mode problems were studied to simulate crack propagation. The agreement between the predicted crack trajectories with those obtained from existing numerical simulation and experiments are excellent.

Acknowledgements

with $b_1 = b_2 = 0.8$ mm surrounding the crack tip was chosen for evaluating the $M^{(1,2)}$ integral for the initial crack. During crack propagation, the domain was moved the same way as explained in Example 3. A plane strain condition was assumed during the analysis.

Fig. 7(a) and (b) shows the comparison of the predicted crack trajectories by using the meshless method for the whole domain and by the proposed method when $L_{EFGM}/L = 11/16$ and $7/16$, with the experimental data in a small region ABCD (see Fig. 6(b)) surrounding the crack. The results in Fig. 7(a) corresponds to $2a = 13.5$ mm and $\gamma = 43°$ and the results in Fig. 7(b) corresponds to $2a = 14.2$ mm and $\gamma = 30°$. In both cases, the increment of crack length at each crack tip during each step of crack propagation was 2% of the initial crack length. The predicted crack trajectories by the proposed method are in good agreement with the experimental results.

8. Summary and conclusions

A coupled meshless-finite element method was developed for analyzing linear-elastic cracked structures subject to mode-I and mixed-mode loading conditions. The EFGM was used to model material behavior close to cracks and the FEM in areas away from cracks. In the interface region, the

References

[1] Lucy L. A numerical approach to testing the fission hypothesis. Astron J 1977;82:1013–24.

[2] Monaghan JJ. An introduction to SPH. Comput Phys Commun 1988;48:89–96.

[3] Libersky LD, Petschek AG, Carney TC, Hipp JR, Alliahdadi FZ. High strain Lagrangian hydrodynamics. J Computat Phys 1993; 109:67–75.

[4] Nayroles B, Touzot G, Villon P. Generalizing the finite element method: diffuse approximation and diffuse elements. Computat Mech 1992;10:307–18.

[5] Belytschko T, Lu YY, Gu L. Element-free Galerkin methods. Int J Numer Meth Engng 1994;37:229–56.

[6] Belytschko T, Lu YY, Gu L. Crack propagation by element-free Galerkin methods. Engng Fracture Mech 1995;51(2):295–315.

[7] Lu YY, Belytschko T, Gu L. A new implementation of the element free Galerkin method. Comput Meth Appl Mech Engng 1994; 113:397–414.

[8] Duarte CAM, Oden JT. H–p clouds — an h–p meshless method. Numer Meth Partial Differential Equations 1996;12(6):673–705.

[9] Melenk JM, Babuska I. The partition of unity finite element method: basic theory and applications. Comput Meth Appl Mech Engng 1996;139:280–314.

[10] Liu WK, Jun S, Zhang YF. Reproducing kernel particle methods. Int J Numer Meth Fluids 1995;20:1081–106.

[11] Liu WK, Li S, Belytschko T. Moving least square kernel Galerkin method – Part I: methodology and convergence. Comput Meth Appl Mech Engng 1997;143:422–33.

[12] Liu WK, Uras RA, Chen Y. Enrichment of the finite element method

with the reproducing kernel particle method. J Appl Mech 1997; 64:861–70.

[13] Krongauz Y, Belytschko T. Enforcement of essential boundary conditions in meshless approximation using finite elements. Comput Meth Appl Mech Engng 1996;131:1335–45.

[14] Hegen D. Element-free Galerkin methods in combination with finite element approaches. Comput Meth Appl Mech Engng 1996;135:143–66.

[15] Huerta A, Fernandez-Mendez S. Enrichment and coupling of the finite element and meshless methods. Int J Numer Meth Engng 2000;48:1615–36.

[16] Lancaster P, Salkauskas K. Surfaces generated by moving least squares methods. Math Comput 1981;37:141–58.

[17] Rao BN, Rahman S. An efficient meshless method for fracture analysis of cracks. Comput Mech 2000;26:398–408.

[18] Zienkiewicz OC, Taylor RL. The finite element method. 4th ed, vols. 1 and 2. New York: McGraw-Hill, 1989.

[19] Fleming M, Chu YA, Moran B, Belytschko T, Lu YY, Gu L. Enriched element-free Galerkin methods for crack-tip fields. Int J Numer Meth Engng 1997;40:1483–504.

[20] Middleton D. An introduction to statistical communication theory. Piscataway, NJ: IEEE Press, 1996.

[21] Organ DJ, Fleming M, Terry T, Belytschko T. Continuous meshless approximations for non-convex bodies by diffraction and transparency. Comput Mech 1996;18:225–35.

[22] Chen JS, Wang HP. New boundary condition treatments in meshfree computation of contact problems. Comput Meth Appl Mech Engng 2000;187(3–4):441–68.

[23] Yau JF, Wang SS, Corten HT. A mixed-mode crack analysis of isotropic solids using conservation laws of elasticity. J Appl Mech 1980;47:335–41.

[24] Moran B, Shih F. Crack tip and associated domain integrals from momentum and energy balance. Engng Fracture Mech 1987;27:615–42.

[25] Erdogan F, Sih GC. On the crack extension in plates under plane loading and transverse shear. J Basic Engng 1963;85:519–27.

[26] Sih GC. Strain–energy–density factor applied to mixed-mode crack problems. Int J Fracture 1974;10:305–21.

[27] Wu CH. Fracture under combined loads by maximum energy release rate criterion. J Appl Mech 1978;45:553–8.

[28] Goldstein RV, Salganik RL. Brittle fracture of solids with arbitrary cracks. Int J Fracture 1974;10:507–27.

[29] Tada H, Paris PC, Irwin GR. The stress analysis of cracks handbook. Hellertown, PA: Del Research Corporation, 1973.

[30] Kaljevic I, Saigal S. An improved element free Galerkin formulation. Int J Numer Meth Engng 1997;40:2953–74.

[31] Wilson WK. Combined mode fracture mechanics, PhD Thesis, University of Pittsburgh, PA, 1969.

[32] Pustejovsky MA. Fatigue crack propagation in titanium under general in-plane loading — I: experiments. Engng Fracture Mech 1979;11:9–15.

[33] Pustejovsky MA. Fatigue crack propagation in titanium under general in-plane loading — II: analysis. Engng Fracture Mech 1979;11:17–31.